



Coexistence of topological type-II Weyl and triply degenerate points in a chiral photonic metamaterial

Mingzhu Li ¹, Jie Song,^{1,*} and Yongyuan Jiang ^{1,2,3,4,†}¹*School of Physics, Harbin Institute of Technology, Harbin 150001, China*²*Collaborative Innovation Center of Extreme Optics, Shanxi University, Taiyuan 030006, China*³*Key Lab of Micro-Optics and Photonic Technology of Heilongjiang Province, Harbin 150001, China*⁴*Key Lab of Micro-Nano Optoelectronic Information System, Ministry of Industry and Information Technology, Harbin 150001, China*

(Received 20 December 2021; accepted 8 February 2022; published 15 February 2022)

In this work, we report the coexistence of type-II Weyl points and triply degenerate points while taking the nonlocal effect into account in a chiral photonic metamaterial system. The chiral effect introduces a break in the spatial inversion symmetry, which is necessary for the generation of nodal points. These nodal points are symmetrically distributed on the k_z axis and possess the time-reversal symmetry-protection mechanism. Remarkably, the projections of all nodal points are connected by a Fermi arc surface state, and it agrees well with the single monopole charges of these nodal points, which demonstrates the topological characteristics of the band degenerate points. We theoretically show that the localized Fermi arc can be formed at the interface between the metamaterial and vacuum, which may improve the compactness of photonic devices. Especially, the nonreciprocal surface waves can propagate forward around the sharp corner without experiencing backscattering, which can be used for the robust transmission of information.

DOI: [10.1103/PhysRevB.105.085304](https://doi.org/10.1103/PhysRevB.105.085304)

I. INTRODUCTION

The study of topological semimetals [1–3] with protected band crossing points has been attracting great interest owing to new physics and potential applications behind them, such as exotic surface states [4,5], topological communication [6], and topological lasers [7–9]. Generally, topological semimetals have three types according to the dimensionality of the band degeneracies: zero-dimensional points [10–12], one-dimensional lines [13–15], and two-dimensional surfaces semimetals [16–18]. Dirac and Weyl points are two typical cases for the zero-dimensional nodal points which correspond to fourfold and twofold band crossing points, respectively [19–21]. In particular, Weyl points originally predicted in high-energy physics was later observed in solid-state materials and appeared in pairs with opposite chirality [22–24]. The different slopes of the crossing bands make nodal points have distinct physical properties in topological semimetals [25–27]. As shown in Fig. 1, the conventional Weyl cone, i.e., type-I Weyl point, has a pointlike Fermi surface. The type-II Weyl point possesses a conical Fermi surface and has a strongly tilted cone dispersion [28], so its physical properties are very different from the type-I Weyl point. Type-II Weyl semimetals have numerous unique transport and optical properties, including antichiral Landau levels [29] and anisotropic chiral anomaly [30]. If one of the two bands forming a Weyl point is flat, the Weyl degeneracy point is exactly at the critical

transition between type-I and type-II Weyl points, which is known as the critical-type Weyl point [31–33].

Recently, in addition to Dirac and Weyl fermions, other exotic new types of topological quasiparticles have been investigated, which can be hosted by threefold, sixfold, or eightfold degenerate points in the band structures, advancing the understanding on band topology and enriching the family of topological materials [34–37]. Notably, the new type of three-component fermions can be viewed as an intermediate phase between the four-component Dirac and the two-component Weyl fermions. Triply degenerate points hold effective integer spin while preserving linear dispersion and Fermi statistics. They also give rise to Fermi arcs when projected onto a certain specific equifrequency surface [38]. The topological property of triply degenerate points can be characterized by the nonzero topological charge [39]. Furthermore, topological semimetals with triply degenerate points are proposed to have intriguing physics in spectroscopic and transport properties, such as exotic Fermi surface transition and large negative magnetoresistance [40–42]. Therefore, a series of topological materials with triply degenerate nodal points have been studied theoretically and experimentally [43,44].

Materials containing multiple topological features have attracted enormous attention in recent years. The physical properties and related applications of various topological semimetals mentioned above have been widely studied in different systems [45–49], such as condensed matter, electromagnetic, and acoustic systems. Meanwhile, a lot of effort has been devoted to searching materials that can possess such novel topologically protected band crossings simultaneously [50–54]. Entanglement among different states sometimes

*jsong@hit.edu.cn

†jiangyy@hit.edu.cn

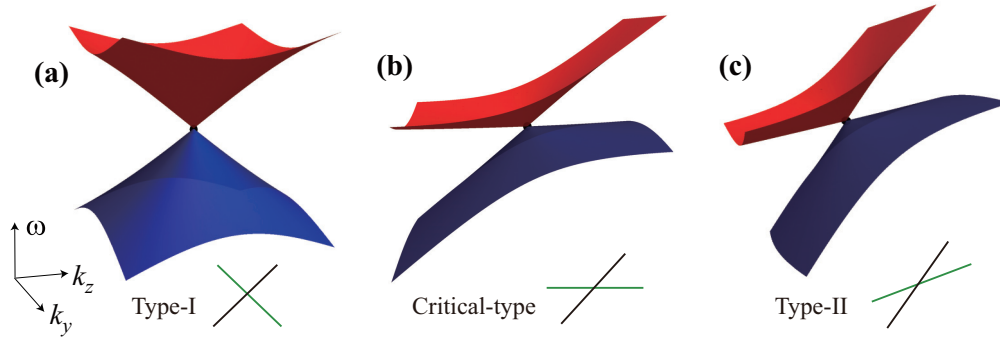


FIG. 1. Types of Weyl semimetals. (a) Illustrations of a conventional Weyl cone and type-I band dispersion; (b) a critical-type Weyl cone band dispersion and (c) a tilted Weyl cone and type-II band dispersion. The following illustration shows the dispersion along the z direction, where the black line and green line correspond to the transverse mode and longitudinal mode, respectively. Only the k_y and k_z axes among the three momenta are drawn due to the limited dimensions.

will bring new phenomena. Typically, the entanglement of superconductivity and topology, that is, topological superconductors, is considered to be the way to realize Majorana fermions [25,55]. For such a consideration, it is meaningful to study the coexistence of different degenerate points in a topological material. This will help us to understand the topological state, deeply study the properties of basic particles, discover novel physical phenomena, and develop new electronic devices. Thus, the potential entanglement between different types of band degenerate points may also be an interesting topic in the future. However, a topological semimetal with both type-II Weyl points and topologically nontrivial triply degenerate points has not been studied in a photonic metamaterial.

In this work, we demonstrate that a photonic chiral metamaterial in the presence of nonlocal effect hosts the type-II Weyl and triply degenerate points simultaneously. When the nonlocal effect is ignored, two pairs of Weyl degeneracy points of the system are exactly at the critical transition between the type-I and type-II Weyl points, i.e., critical-type Weyl points. While taking the nonlocal effect into account, the bulk plasmon dispersion tilts upward, which forms the type-II Weyl points and triply degenerate points. As an important signature of the inherent property of the topological semimetals, the nontrivial Fermi arc surface state exists at the interface between the chiral metamaterial and vacuum. COMSOL Multiphysics is used to prove the field localization on the boundary of the Fermi arc. In addition, the surface waves are confirmed to be topologically protected, which can bypass sharp defects by numerical simulations. Particularly, to clarify the coexistence conditions of these nodal points, we explore and discuss the phase diagram in chiral metamaterial with the nonlocal effect. The coexistence of type-II Weyl and triply degenerate points in the chiral metamaterial reveals a promising platform for studying the interplay between these exotic properties and the topological band crossings.

This paper is organized as follows. In Sec. II, we prove the coexistence of type-II Weyl and triply degenerate points in a chiral metamaterial. In Sec. III, we exhibit the existence of localized Fermi arc surface state. In Sec. IV, COMSOL Multiphysics simulation shows that the Fermi arc is topologically protected, and the surface waves can bypass defects for

unidirectional robust transmission. In Sec. V, we give the phase diagram in chiral metamaterial while considering the nonlocal effect. The conclusion is given in Sec. VI.

II. PHOTONIC TYPE-II WEYL POINTS AND TRIPLY DEGENERATE POINTS IN A CHIRAL METAMATERIAL

In order to break the spatial inversion symmetry, the chiral metamaterial with unit cell composed of metallic helical elements would be a good candidate [56]. To simultaneously realize the electric and magnetic longitudinal modes, metallic helical elements are generally utilized to introduce both electric and magnetic resonances along the z direction [12,56]. Moreover, the nonlocal effect will bring about the positive dispersion for longitudinal plasmonic mode [15,57]. Here, we consider a metamaterial with the following tensors of relative permittivity, permeability, and chirality: $\bar{\epsilon} = \text{diag}(\epsilon_t, \epsilon_t, \epsilon_z)$, $\bar{\mu} = \text{diag}(\mu_t, \mu_t, \mu_z)$, $\bar{\xi} = \text{diag}(\gamma, \gamma, 0)$, where $\epsilon_z = 1 - \omega_{ep}^2/\omega^2$ and $\mu_z = 1 - \omega_{mp}^2/\omega^2 + \beta k_z^2$ [32] possess Drude's dispersion. ω , ω_{ep} , ω_{mp} , γ , and β are the angular frequency, effective plasma frequency, magnetic plasma frequency, chirality parameter, and nonlocal parameter, respectively.

The constitutive relations of the medium are given as

$$\begin{pmatrix} \mathbf{D} \\ \mathbf{B} \end{pmatrix} = \begin{pmatrix} \epsilon_0 \bar{\epsilon} & i\sqrt{\epsilon_0 \mu_0} \bar{\xi} \\ -i\sqrt{\epsilon_0 \mu_0} \bar{\xi} & \mu_0 \bar{\mu} \end{pmatrix} \begin{pmatrix} \mathbf{E} \\ \mathbf{H} \end{pmatrix}, \quad (1)$$

where ϵ_0 and μ_0 are the permittivity and permeability of vacuum, respectively.

Combining $\nabla \times \mathbf{E} = i\omega \mathbf{B}$ and $\nabla \times \mathbf{H} = -i\omega \mathbf{D}$, Maxwell's equations can be recast to a 6-by-6 matrix form

$$\left[\begin{pmatrix} i\bar{\kappa} & 0 \\ 0 & i\bar{\kappa} \end{pmatrix} - i\omega \begin{pmatrix} \bar{\mathbf{I}} & 0 \\ 0 & -\bar{\mathbf{I}} \end{pmatrix} \begin{pmatrix} -\sqrt{\epsilon_0 \mu_0} \bar{\xi} & \mu_0 \bar{\mu} \\ \epsilon_0 \bar{\epsilon} & \sqrt{\epsilon_0 \mu_0} \bar{\xi} \end{pmatrix} \right] \begin{pmatrix} \mathbf{E} \\ \mathbf{H} \end{pmatrix} = 0, \quad (2)$$

where $\bar{\kappa} = [0, -k_z, k_y; k_z, 0, -k_x; -k_y, k_x, 0]$ is the antisymmetric tensor and $\bar{\mathbf{I}}$ is the identity tensor matrix. For the sake of simplicity, ω is normalized to ω_{mp} and the wave vectors \mathbf{k} are normalized to k_m ($k_m = \omega_{mp}/c$, c is the speed of light in vacuum). In addition, we assume $\epsilon_t = \mu_t = 1$, $\omega_{mp} = 1$, $\omega_{ep} = 2\omega_{mp}$, and $\gamma = 1$ in the present study.

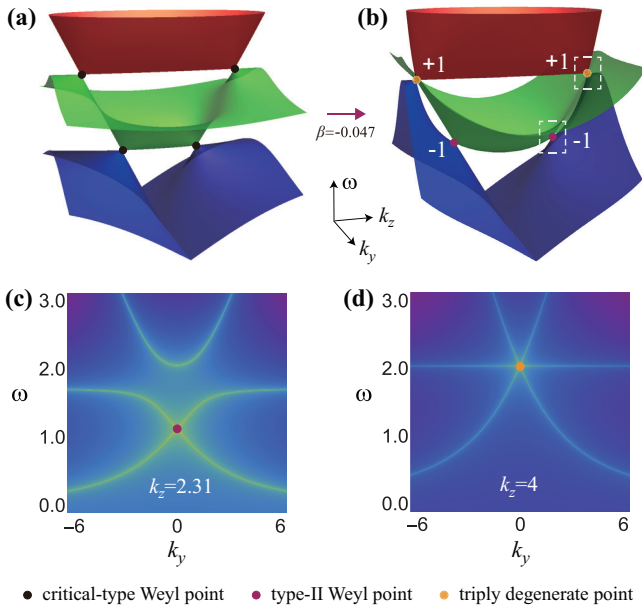


FIG. 2. The dispersion relation of band structure and the locations of degenerate points for chiral metamaterial with different nonlocal parameters. (a) $\beta = 0$ and (b) $\beta = -0.047$. The other electromagnetic parameters are the same. The black, purple, and orange dots indicate the critical-type Weyl points, type-II Weyl points, and triply degenerate points, respectively. Panels (c) and (d) give the dispersion along the k_y direction, k_z is fixed at the type-II Weyl point ($k_z = 2.31$) and the triply degenerate point ($k_z = 4$), respectively.

The bulk state equation of metamaterial can be described by the electric field \mathbf{E} . Figure 2 presents the dispersion relation of band structure with different electromagnetic parameters. It is clearly shown that there are three bands from low frequency to high frequency and four linear degeneracies along the k_z axis. The chiral metamaterial hosts two pairs of Weyl points in total. In physical terms, Weyl points are monopoles of the Berry curvature in three-dimensional momentum space, which are protected by the orthogonality of the polarizations, i.e., the bulk plasmon and the circularly polarized propagating modes [57].

When the nonlocal effect is ignored, i.e., $\beta = 0$, Weyl points in the proposed system are exactly at the critical transition between the type-I and type-II Weyl points, as shown in Fig. 2(a). The topological property of the Weyl point can be characterized by Chern numbers [57,58]. We note that in a system with time-reversal symmetry, one pair of Weyl points at \mathbf{k} and $-\mathbf{k}$ have the same topological charge, because the Berry curvature satisfies $\mathbf{\Omega}(\mathbf{k}) = -\mathbf{\Omega}(-\mathbf{k})$ [12,39] in the chiral medium. After the time-reversal operator is applied to one of the two Weyl points, the other Weyl point with the same topological charge can be yielded. As shown in Fig. 2, triply degenerate points and Weyl points are highlighted by the colored dots. The black, purple, and orange dots indicate the critical-type Weyl points, type-II Weyl points, and triply degenerate points, respectively.

When the nonlocal parameter is set as $\beta = -0.047$, as shown in Fig. 2(b), the energy bands in low frequencies tilt upward and degenerate with that in high frequency, which generates triply degenerate points. Compared with Fig. 2(a),

the nonlocal effect in the chiral metamaterial generates triply degenerate points. Nonlocality does not affect the symmetry-protection mechanism of the system [5]. Therefore, these newly generated triply degenerate points are also protected by the time-reversal symmetry. In addition, it is worth noting that there is still degeneracy for energy bands in low frequencies. However, due to the inclination of the energy band, the degenerate points become the type-II Weyl points. Triply degenerate points and type-II Weyl points are represented by orange and purple points respectively, the positive ($C = +1$) and negative ($C = -1$) chirality of the corresponding points is marked in Fig. 2(b). The energy dispersion in the vicinity of the type-II Weyl points forms a tilted cone. Type-II Weyl semimetals exhibit novel transport properties different from normal Weyl semimetals [28,59], such as the anomalous Hall effect, anisotropy of the dynamical conductivity, and the collapse of Landau levels. In order to show the degeneracy of bands more clearly, as depicted in Figs. 2(c) and 2(d), we give the dispersion along the k_y direction, while k_z is fixed at the type-II Weyl point ($k_z = 2.31$) and the triply degenerate point ($k_z = 4$), respectively.

Triply degenerate points and Weyl points coexist in the chiral metamaterial while taking the nonlocal effect into account. As shown in the white dotted boxes in Fig. 2(b), we focus on the topological characteristics of degenerate points at the positive k_z region. The dispersion relations around the triply degenerate points and Weyl points are analyzed in detail, as shown in Fig. 3. The dispersion is along the z direction, where the black arrow and cyan/yellow arrows correspond to the transverse and longitudinal modes, respectively. As depicted in Fig. 3(a), the dispersion in the ω - k_z plane is presented at $k_x = k_y = 0$. The dispersions of the longitudinal electric mode and longitudinal magnetic mode are determined by

$$\epsilon_z = 1 - \omega_{ep}^2/\omega^2 = 0, \quad \mu_z = 1 - \omega_{mp}^2/\omega^2 + \beta k_z^2 = 0. \quad (3)$$

The transverse mode is expressed by

$$k_z^4 + \omega^4(\gamma^2 - \epsilon_t \mu_t)^2 - 2\omega^2 k_z^2(\gamma^2 + \epsilon_t \mu_t) = 0. \quad (4)$$

The degeneracy between the transverse mode and the longitudinal magnetic mode leads to the generation of type-II Weyl points (purple dots). Notably, the degeneracy of one transverse mode and two longitudinal modes will produce triply degenerate points (orange dots).

Since the system has rotational invariance in the x - y plane, the dispersion profiles near degenerate points in wave vector space k_x - k_z and k_y - k_z are the same. The band dispersions are linear in three-dimensional momentum space along all directions, as illustrated in Fig. 3. The band structure of the triply degenerate points in the ω - k_x - k_y surface is shown in Fig. 3(b). It is clear that two bands have linear dispersion along an arbitrary momentum direction, like that in a Weyl cone, while the third energy band remains flat. As depicted in Fig. 3(c), triply degenerate points are formed by the crossing of three nondegenerate bands. On the other hand, the Weyl point possesses a conical structure with doubly degenerate linear band crossings, as shown in Fig. 3(d). It can be seen intuitively that the two bands in low frequencies tilt upward to form a type-II Weyl point in Fig. 3(e). The group velocities around the Weyl point along the z direction have the same

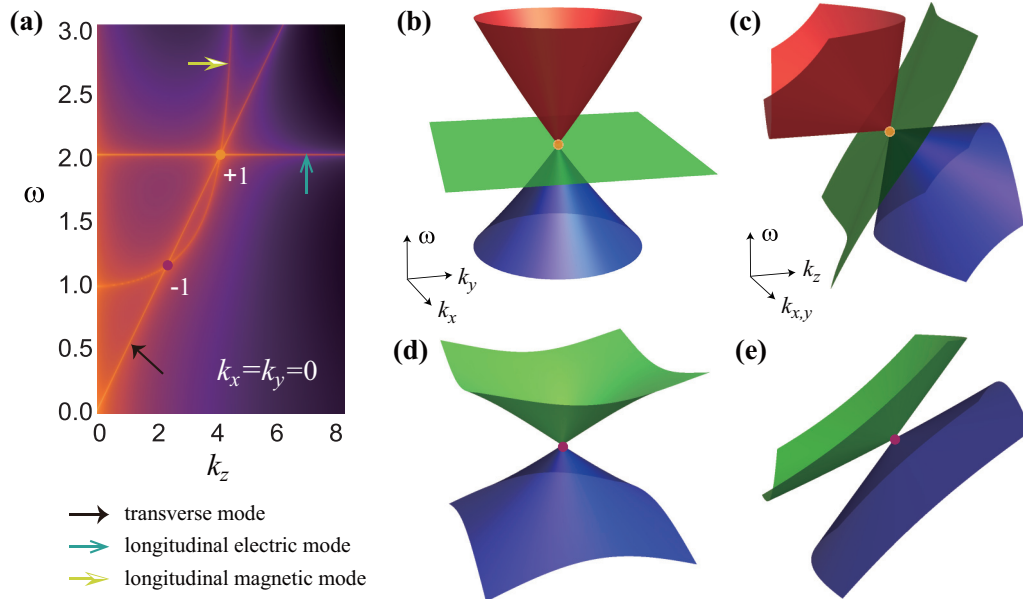


FIG. 3. The band structure of the bulk states. (a) The dispersion along the z direction of a chiral metamaterial with the nonlocal parameter $\beta = -0.047$. The horizontal line represents the dispersion of the longitudinal electric mode. The black and yellow arrows correspond to the transverse mode and longitudinal magnetic mode, respectively. The band dispersions of triply degenerate points and Weyl points in the k_x - k_y plane with (b) $\omega = \omega_{ep}$ and (d) $\omega = \omega_{mp}$. Panels (c) and (e) give the band dispersions of triply degenerate points and Weyl points in the ω - k plane.

sign, which is indeed a unique feature of the type-II Weyl point [28].

III. FERMI ARC EXISTS AT THE INTERFACE BETWEEN THE CHIRAL METAMATERIAL AND VACUUM

A landmark feature of the Weyl topological phase is the presence of exotic surface states with Fermi arc. In the above discussions, we have seen that there exist triply degenerate points with positive charge $C = +1$ and type-II Weyl points with negative charge $C = -1$. According to the bulk-edge correspondence [60], there should be a Fermi arc connecting degenerate points at different positions. Therefore, it is important to examine and compare their surface consequences.

For photons, the vacuum is not an insulator. Different from electronic materials, there are photonic bands in the vacuum. Here, in order to study the topological connectivity characteristics of Fermi arc, we take the y - z plane ($x = 0$) to be the interface between vacuum ($x > 0$) and the chiral metamaterials ($x < 0$). Then, according to the electromagnetic boundary continuity condition, the surface wave equation can be obtained by numerical calculation [43].

Next, we focus on the dispersion of the bulk state and Fermi arc near the type-II Weyl and triply degeneracy frequencies. The six equipfrequency contours containing both bulk and surface states on the k_y - k_z plane are shown in Fig. 4. Dispersions of the Fermi arc are represented by the black solid curves at (a) $\omega = 2.02$, (b) $\omega = 2$, (c) $\omega = 1.98$, (d) $\omega = 1.25$, (e) $\omega = 1.15$, and (f) $\omega = 1$, respectively. As shown in Fig. 4(b), two orange dots at large wave vector k represent one pair of triply degenerate points carrying positive chirality. Figures 4(a) and 4(c) correspond to the frequency

above and below the triply degenerate points. Although great changes have taken place in the bulk equipfrequency surfaces, it is straightforward to show that a Fermi arc emerges from the triply degenerate point and tangentially terminates at the light cone. This clearly verifies the existence of single topological charge of the triply degenerate point.

One pair of type-II Weyl points with negative chirality at lower frequency is represented by the purple dots, as depicted in Fig. 4(e). Nontrivial Fermi arc surface states between the type-II Weyl point partners are shown in Figs. 4(d)–4(f). It serves as an important signature of the topological nature of the system. At the Weyl degeneracy frequency $\omega = 1.15$, the projection of two type-II Weyl points are connected by one Fermi arc, as illustrated in Fig. 4(e). It also agrees with the single topological charge of type-II Weyl points. In addition, at frequencies slightly shifted away from the Weyl frequency [shown as Figs. 4(d) and 4(f)], a k -space gap appears between the two bulk states. However, the Fermi arc always exists and remains connected. With the increase of frequency ω , the bulk state of metamaterial would encircle the vacuum at a certain value of ω . Thus, the nontrivial Fermi arc surface state is tangent to the bulk mode of metamaterial instead of the vacuum state, as shown in Fig. 4(d). In short, the bulk equipfrequency surfaces change significantly at different frequencies, the Fermi arc still exists, and is tangent to either metamaterial or vacuum bulk mode depending on the frequency ω . From each degenerate point, there is a Fermi arc connecting to the bulk state of vacuum or metamaterial.

To verify the nontrivial topological properties of the Fermi arc, as shown in Figs. 4(c) and 4(f), we select two different propagation constants $k_z = 3$ and $k_z = 1.5$, which are expressed by the points A and B , respectively. It is shown that

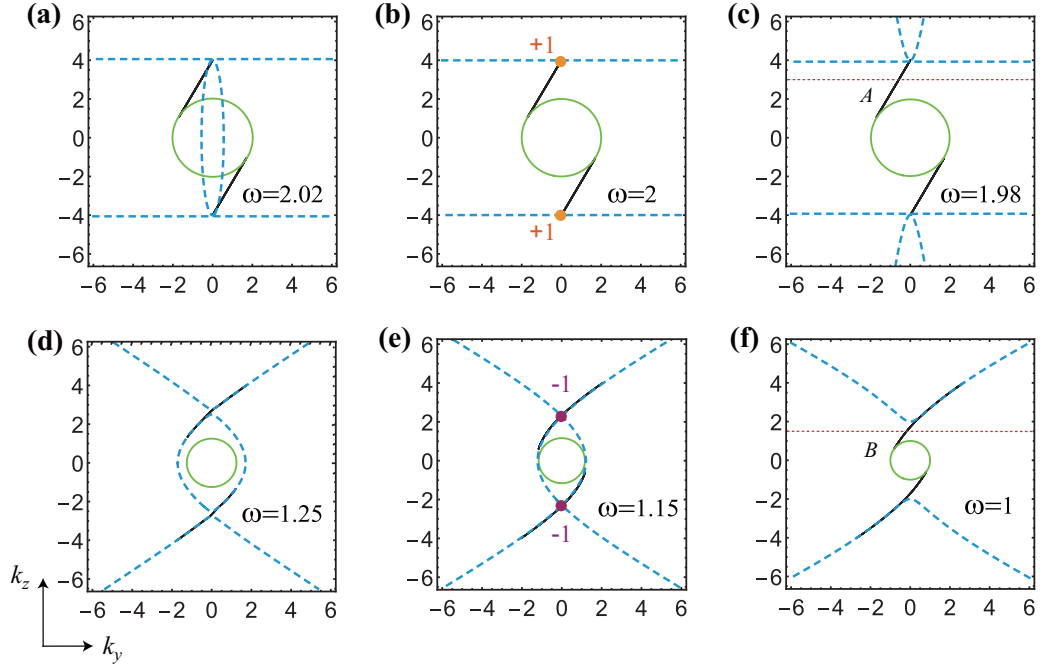


FIG. 4. Equifrequency contours containing both bulk and Fermi arc surface states on the k_y - k_z plane at (a) $\omega = 2.02$, (b) $\omega = 2$, (c) $\omega = 1.98$, (d) $\omega = 1.25$, (e) $\omega = 1.15$, and (f) $\omega = 1$. Black solid curves, green solid lines, and blue dashed lines represent the dispersion of Fermi arc, the vacuum state, and the bulk state of the chiral metamaterial, respectively. The type-II Weyl points and triply degenerate points are highlighted by the purple and orange dots, respectively.

these surface modes are localized. Moreover, as illustrated in Figs. 5(a) and 5(c), the amplitude of the Fermi arc surface states will decay rapidly away from the boundary. It indicates

these surface waves are confined on the interface. Figures 5(b) and 5(d) show the field distribution diagrams of the surface modes at the interface between the metamaterial and vacuum. The results herein can improve the compactness of photonic devices and facilitate the integration of photonic circuits.

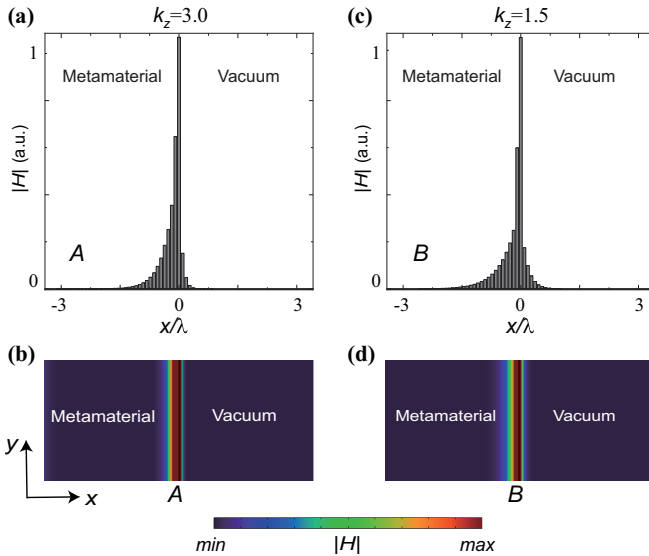


FIG. 5. The Fermi arc surface states exist localized field mode at the interface between the chiral metamaterial ($x < 0$) and vacuum ($x > 0$). The values of two different propagation constants k_z at points A and B are (a) $k_z = 3$ and (c) $k_z = 1.5$, respectively. (b),(d) The simulated $|H|$ field distributions are shown by COMSOL Multiphysics. The fields are localized at the interface for points A and B.

IV. TOPOLOGICALLY PROTECTED FERMI ARC SURFACE STATES

The topological properties and the corresponding Fermi arc surface states in the chiral metamaterial are proved by numerical simulation. As exhibited in Figs. 6(a) and 6(b), the 2D equal-frequency surfaces ($\omega = 1.98$ and $\omega = 1$) of the metamaterial are illustrated by blue color. Since the surface state is in direct contact with the vacuum, the vacuum effect should be taken into account. The green region represents the vacuum state. The topologically protected Fermi arc surface state (black curve) exists at the interface between the vacuum ($x > 0$) and metamaterial ($x < 0$). Then, we choose three different values of propagation constants k_z at points B, C, and D for $\omega = 1$, which correspond to (d) $k_z = 1.5$, (e) $k_z = 0.95$, and (f) $k_z = 2$, respectively. Another point A [Figs. 4(c) and 6(a)] represents $k_z = 3$ and $\omega = 1.98$. As shown in Fig. 6(c), simulation is performed in the x - y plane, z component of the magnetic field of surface waves at $\omega = 1.98$, which confirms the surface wave propagates unidirectionally on the boundary without experiencing backscattering at the sharp corners.

It is similar to point A in Fig. 6(c), because the propagation constant k_z of point B is also located in the middle of the gap, and the backward scattering-immune unidirectional transmission can be obtained, as shown in Fig. 6(d). This

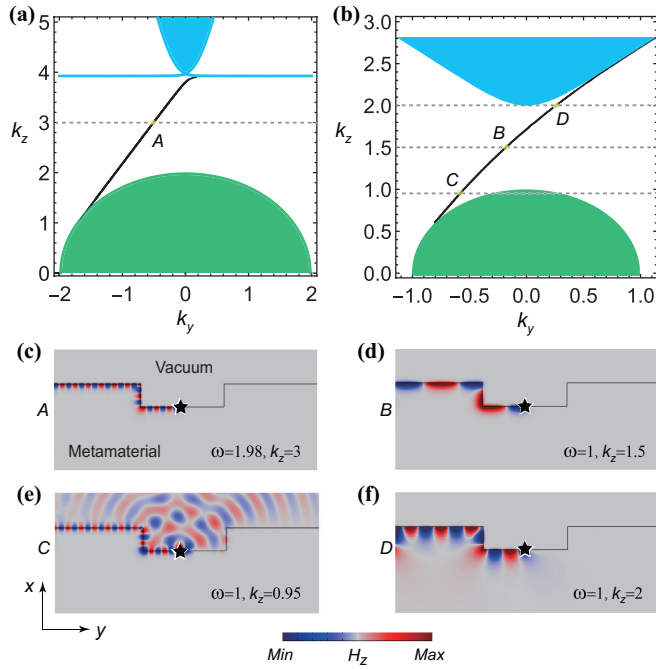


FIG. 6. COMSOL simulation for the surface modes at the interface between the vacuum ($x > 0$) and chiral metamaterial ($x < 0$). Panels (a) and (b) describe the 2D equal-frequency surfaces and Fermi arcs (black curves) for $\omega = 1.98$ and $\omega = 1$, respectively. Four different propagation constants k_z at the points A, B, C, and D are (c) $k_z = 3$, (d) $k_z = 1.5$, (e) $k_z = 0.95$, and (f) $k_z = 2$, respectively. The green region represents the vacuum state and the blue one is the bulk state of the metamaterial. Panels (c)–(f) give the simulated surface waves transportation results corresponding to the cases in (a) and (b), show the field patterns H_z from simulation, and share the same color map. Black stars denote the dipole sources for exciting the surface waves.

means that the surface wave cannot propagate in the interior of the medium, but only along the surface of the medium. In addition, comparing Figs. 6(c) and 6(d), the amplitudes of the magnetic field z components at points A and B change because the selected propagation constants k_z are different. On the other hand, since neither point C nor point D is located in the common gap region, the surface waves are scattered into the bulk states by sharp defects. Specifically, the surface state for point C is very close to the equifrequency contour surfaces of vacuum, so the surface wave diffuses into vacuum, as shown in Fig. 6(e). Similarly, the surface wave can also be scattered to the bulk state of metamaterial for point D, as illustrated in Fig. 6(f). Therefore, numerical simulations show that nonreciprocal propagation of the surface waves is confirmed to be topologically protected. The topological origin of the unidirectional transmission waves is due to the existence of only one Fermi arc in the gap region [Figs. 6(a) and 6(b)].

V. PHASE DIAGRAM IN CHIRAL METAMATERIAL WITH CONSIDERING THE NONLOCAL EFFECT

In the previous discussion, the nonlocal parameter $\beta = -0.047$ is an example to analyze the coexistence of type-II

Weyl points and triply degenerate points. Since we are interested in studying the coexistence of these nodal points, we further explore and discuss the phase diagram in chiral metamaterial while considering the nonlocal effect. Equations (3) and (4) give the dispersion relations for the longitudinal electric mode, longitudinal magnetic mode, and transverse mode, respectively.

Combining $\mu_z = 1 - \omega_{mp}^2/\omega^2 + \beta k_z^2 = 0$ [Eq. (3)] and $k_z^4 + \omega^4(\gamma^2 - \epsilon_t \mu_t)^2 - 2\omega^2 k_z^2(\gamma^2 + \epsilon_t \mu_t) = 0$ [Eq. (4)], we can obtain the relation between the wave vector k_z and the nonlocal parameter β as

$$k_z^\pm = \frac{\sqrt{-1 \pm \sqrt{1 + 4\omega_{mp}^2 \beta (\gamma + \sqrt{\epsilon_t \mu_t})^2}}}{\sqrt{2\beta}}. \quad (5)$$

Equation (5) represents the degeneracy of the longitudinal magnetic mode and the transverse mode, as shown by the red solid lines in Fig. 7(a). The critical value for the nonlocal parameter $\beta = -1/(4\omega_{mp}^2(\gamma + \sqrt{\epsilon_t \mu_t})^2) = -0.0625$ is shown by the red dotted line. Grey ($-0.0625 < \beta < 0$) and khaki ($\beta < -0.0625$) shaded areas represent the presence and absence of the coexistence of these nodal points, respectively. The longitudinal magnetic mode and transverse mode degenerate along the k_z axis when the nonlocal parameter satisfies $-0.0625 < \beta < 0$ (gray shaded part). In this case, there are four type-II Weyl points in the system. Specifically, one pair of Weyl points has the small $|k_z|$ value, and the other pair possesses the large $|k_z|$ value. Correspondingly, the two Weyl degeneracy frequencies are also different.

In addition, it can be intuitively found that the dispersion relation of the longitudinal electric mode is flat ($\epsilon_z = 1 - \omega_{ep}^2/\omega^2 = 0$). Further tuning the electric plasma frequency to be equal to one of the two Weyl degeneracy frequencies leads to the creation of two triply degenerate points. Therefore, the system supports two type-II Weyl points and two triply degenerate points. As illustrated in Fig. 7(a), in order to better clarify the effect of nonlocal parameter β on the coexistence of these nodal points, we choose two cases for comparison. The green and blue dashed lines correspond to $\beta = -0.03$ and $\beta = -0.08$, respectively.

As illustrated in Fig. 7(b), we give the dispersion relation of band structure for chiral metamaterial with the nonlocal parameter $\beta = -0.03$ in the ω - k_z plane. Other electromagnetic parameters are $\epsilon_t = \mu_t = 1$, $\gamma = 1$, $\omega_{mp} = 1$ and $\omega_{ep} = \omega_{mp}/\sqrt{1 + (-1 - \sqrt{1 + 4\omega_{mp}^2 \beta (\gamma + \sqrt{\epsilon_t \mu_t})^2})/2} = 2.68$. The degeneracy of the modes clearly shows that the system supports both type-II Weyl points and triply degenerate points. Moreover, similar to $\beta = -0.047$ in Figs. 2(b) and 3(a), the Weyl point here is also located in the low frequency region, while the triply degenerate point lies in the high frequency region, as illustrated in Fig. 7(b). The purple and orange dots indicate the type-II Weyl points and triply degenerate points, respectively. On the contrary, because the nonlocal parameter $\beta = -0.08$ is located in the khaki region, there is no degeneracy between the longitudinal magnetic mode and the transverse mode. No matter how the electric plasma frequency is changed, the three modes cannot cross at the same point,

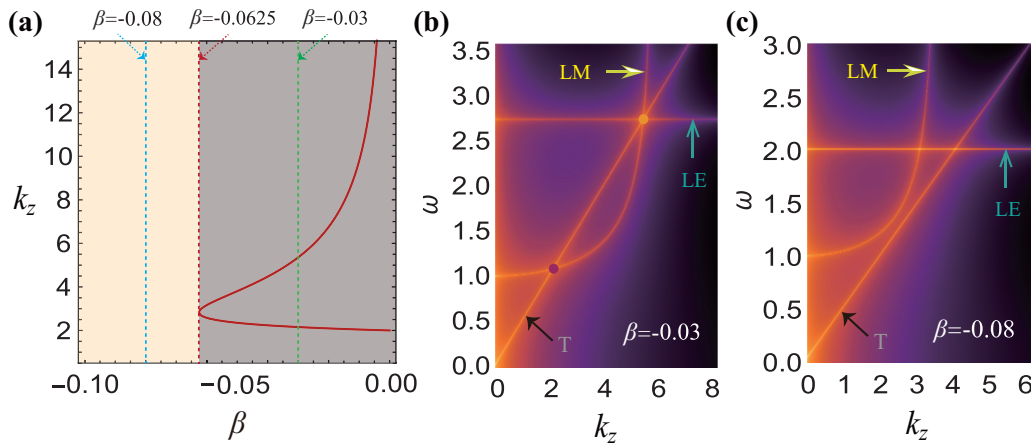


FIG. 7. (a) Phase diagram in the chiral metamaterial while considering the nonlocal effect. The red dotted line represents the critical value of the coexistence of type-II Weyl points and triply degenerate points (the nonlocal parameter $\beta = -0.0625$). Grey and khaki shaded areas indicate the presence and absence of the coexistence of these nodal points, respectively. Panels (b) and (c) show the dispersion along the z direction of the chiral metamaterials when the nonlocal parameters are set as $\beta = -0.03$ and $\beta = -0.08$, respectively. The horizontal line represents the dispersion of the longitudinal electric mode (LE). The black and yellow arrows correspond to the transverse mode (T) and longitudinal magnetic mode (LM), respectively.

that is, the triply degenerate point cannot be generated, as explained in Fig. 7(c).

VI. CONCLUSIONS

In conclusion, we demonstrate that a photonic chiral metamaterial can support critical-type Weyl points owing to the chiral effect. Taking the nonlocal effect into account, the longitudinal magnetic mode slopes upward, and it crosses with the transverse mode and the longitudinal electric mode, which forms triply degenerate points. Meanwhile, the Weyl point in low frequency also changes to type-II. The dispersion relation of the bulk state of the chiral metamaterial can be used to prove the coexistence of these nodal points. More importantly, as a significant embodiment of the nontrivial properties of topological semimetals, there is a photonic Fermi arc surface state at the interface. Due to the single monopole charges of type-II Weyl points and triply degenerate points, the projections of all nodal points are connected by one Fermi arc. This is why the surface wave only travels in one direction.

Moreover, we theoretically proved that the Fermi arc has field localization properties at the interface between the metamaterial and vacuum, thereby it may lead to potential applications in integrated photonic circuits. Notably, it is verified that the Fermi arc surface states are topologically protected. The nonreciprocal surface waves can transmit forward around the sharp corners without backscattering. Interestingly, we show the conditions for the coexistence of type-II Weyl points and triply degenerate points based on the phase diagram of the system. Our work is conducive to a deep understanding of the properties of basic particles, discovering exotic physical phenomena, and providing a prototype platform for exploring the coexistence of multiple topological nodal points.

ACKNOWLEDGMENTS

This work was financially supported by the National Natural Science Foundation of China under Grant No. 62075048 and the Natural Science Foundation of Shandong Province under Grant No. ZR2020MF129.

The authors declare no conflict of interest.

-
- [1] B. Yan and C. Felser, Topological materials: Weyl semimetals, *Annu. Rev. Condens. Matter Phys.* **8**, 337 (2017).
 - [2] A. A. Burkov, Weyl metals, *Annu. Rev. Condens. Matter Phys.* **9**, 359 (2018).
 - [3] J. Hu, S. Xu, N. Ni, and Z. Mao, Transport of topological semimetals, *Annu. Rev. Mater. Res.* **49**, 207 (2019).
 - [4] H. Cheng, W. Gao, Y. Bi, W. Liu, Z. Li, Q. Guo, Y. Yang, O. You, J. Feng, H. Sun, J. Tian, S. Chen, and S. Zhang, Vortical Reflection and Spiraling Fermi Arcs with Weyl Metamaterials, *Phys. Rev. Lett.* **125**, 093904 (2020).
 - [5] B. Yang, Q. Guo, B. Tremain, R. Liu, L. E. Barr, Q. Yan, W. Gao, H. Liu, Y. Xiang, J. Chen, C. Fang, A. Hibbins, L. Lu, and S. Zhang, Ideal Weyl points and helicoid surface states in artificial photonic crystal structures, *Science* **359**, 1013 (2018).
 - [6] Y. Yang, Y. Yamagami, X. Yu, P. Pitchappa, J. Webber, B. Zhang, M. Fujita, T. Nagatsuma, and R. Singh, Terahertz topological photonics for on-chip communication, *Nat. Photonics* **14**, 446 (2020).
 - [7] H. Hübener, M. A. Sentef, U. D. Giovannini, A. F. Kemper, and A. Rubio, Creating stable Floquet-Weyl semimetals by laser-driving of 3D Dirac materials, *Nat. Commun.* **8**, 13940 (2017).
 - [8] B. Bahari, A. Ndao, F. Vallini, A. E. Amili, Y. Fainman, and B. Kanté, Nonreciprocal lasing in topological cavities of arbitrary geometries, *Science* **358**, 636 (2017).

- [9] R. M. A. Dantas, Z. Wang, P. Surówka, and T. Oka, Nonperturbative topological current in Weyl and Dirac semimetals in laser fields, *Phys. Rev. B* **103**, L201105 (2021).
- [10] B. A. Bernevig, It's been a Weyl coming, *Nat. Phys.* **11**, 698 (2015).
- [11] N. P. Armitage, E. J. Mele, and A. Vishwanath, Weyl and Dirac semimetals in three-dimensional solids, *Rev. Mod. Phys.* **90**, 015001 (2018).
- [12] S. Ma, Y. Bi, Q. Guo, B. Yang, O. You, J. Feng, H. Sun, and S. Zhang, Linked Weyl surfaces and Weyl arcs in photonic metamaterials, *Science* **373**, 572 (2021).
- [13] R. Yu, H. Weng, Z. Fang, X. Dai, and X. Hu, Topological Node-Line Semimetal and Dirac Semimetal State in Antiperovskite Cu_3PdN , *Phys. Rev. Lett.* **115**, 036807 (2015).
- [14] L. Xia, Q. Guo, B. Yang, J. Han, C. X. Liu, W. Zhang, and S. Zhang, Observation of Hourglass Nodal Lines in Photonics, *Phys. Rev. Lett.* **122**, 103903 (2019).
- [15] W. Gao, B. Yang, B. Tremain, H. Liu, Q. Guo, L. Xia, A. P. Hibbins, and S. Zhang, Experimental observation of photonic nodal line degeneracies in metacrystals, *Nat. Commun.* **9**, 950 (2018).
- [16] W. Wu, Y. Liu, S. Li, C. Zhong, Z.-M. Yu, X.-L. Sheng, Y. X. Zhao, and S. A. Yang, Nodal surface semimetals: Theory and material realization, *Phys. Rev. B* **97**, 115125 (2018).
- [17] M. Kim, D. Lee, D. Lee, and J. Rho, Topologically nontrivial photonic nodal surface in a photonic metamaterial, *Phys. Rev. B* **99**, 235423 (2019).
- [18] Y. Yang, J. Xia, H. Sun, Y. Ge, D. Jia, S. Yuan, S. A. Yang, Y. Chong, and B. Zhang, Observation of a topological nodal surface and its surface-state arcs in an artificial acoustic crystal, *Nat. Commun.* **10**, 5185 (2019).
- [19] H. Cheng, Y. Sha, R. Liu, C. Fang, and L. Lu, Discovering Topological Surface States of Dirac Points, *Phys. Rev. Lett.* **124**, 104301 (2020).
- [20] W. Wu, Z. Yu, X. Zhou, Y. X. Zhao, and S. A. Yang, Higher-order Dirac fermions in three dimensions, *Phys. Rev. B* **101**, 205134 (2020).
- [21] Y. Yang, Z. Gao, X. Feng, Y. Huang, P. Zhou, S. A. Yang, Y. Chong, and B. Zhang, Ideal Unconventional Weyl Point in a Chiral Photonic Metamaterial, *Phys. Rev. Lett.* **125**, 143001 (2020).
- [22] A. A. Burkov, Topological semimetals, *Nat. Mater.* **15**, 1145 (2016).
- [23] X. Huang, W. Deng, F. Li, J. Lu, and Z. Liu, Ideal Type-II Weyl Phase and Topological Transition in Phononic Crystals, *Phys. Rev. Lett.* **124**, 206802 (2020).
- [24] L. Lu, Z. Wang, D. Ye, L. Ran, L. Fu, J. D. Joannopoulos, and M. Soljačić, Experimental observation of Weyl points, *Science* **349**, 622 (2015).
- [25] L. Xu, X. Zhang, W. Meng, T. He, Y. Liu, X. Dai, Y. Zhang, and G. Liu, Centrosymmetric TiS as a novel topological electronic material with coexisting type-I, type-II and hybrid nodal line states, *J. Mater. Chem. C* **8**, 14109 (2020).
- [26] D. Li, B. Rosenstein, B. Y. Shapiro, and I. Shapiro, Effect of the type-I to type-II Weyl semimetal topological transition on superconductivity, *Phys. Rev. B* **95**, 094513 (2017).
- [27] M. Li, J. Song, and Y. Jiang, Topological characteristic of Weyl degeneracies in a reciprocal chiral metamaterials system, *New J. Phys.* **23**, 093036 (2021).
- [28] A. A. Soluyanov, D. Gresch, Z. Wang, Q. Wu, M. Troyer, X. Dai, and B. A. Bernevig, Type-II Weyl semimetals, *Nature (London)* **527**, 495 (2015).
- [29] Z. Yu, Y. Yao, and S. A. Yang, Predicted Unusual Magnetoresponse in Type-II Weyl Semimetals, *Phys. Rev. Lett.* **117**, 077202 (2016).
- [30] G. Sharma, P. Goswami, and S. Tewari, Chiral anomaly and longitudinal magnetotransport in type-II Weyl semimetals, *Phys. Rev. B* **96**, 045112 (2017).
- [31] W. Gao, B. Yang, M. Lawrence, F. Fang, B. Béri, and S. Zhang, Photonic Weyl degeneracies in magnetized plasma, *Nat. Commun.* **7**, 12435 (2016).
- [32] M. Xiao, Q. Lin, and S. Fan, Hyperbolic Weyl Point in Reciprocal Chiral Metamaterials, *Phys. Rev. Lett.* **117**, 057401 (2016).
- [33] M. Li, J. Song, and Y. Jiang, Photonic topological Weyl degeneracies and ideal type-I Weyl points in the gyromagnetic metamaterials, *Phys. Rev. B* **103**, 045307 (2021).
- [34] S. Bao, J. Wang, W. Wang, Z. Cai, S. Li, Z. Ma, D. Wang, K. Ran, Z. Dong, D. L. Abernathy, S. Yu, X. Wan, J. Li, and J. Wen, Discovery of coexisting Dirac and triply degenerate magnons in a three-dimensional antiferromagnet, *Nat. Commun.* **9**, 2591 (2018).
- [35] S. A. Owerre, Magnonic triply-degenerate nodal points, *Europhys. Lett.* **120**, 57002 (2017).
- [36] T. Zhang, Z. Song, A. Alexandradinata, H. Weng, C. Fang, L. Lu, and Z. Fang, Double-Weyl Phonons in Transition-Metal Monosilicides, *Phys. Rev. Lett.* **120**, 016401 (2018).
- [37] Z. Yu, W. Wu, Y. X. Zhao, and S. A. Yang, Circumventing the no-go theorem: A single Weyl point without surface Fermi arcs, *Phys. Rev. B* **100**, 041118(R) (2019).
- [38] H. Yang, J. Yu, S. S. P. Parkin, C. Felser, C. Liu, and B. Yan, Prediction of Triple Point Fermions in Simple Half-Heusler Topological Insulators, *Phys. Rev. Lett.* **119**, 136401 (2017).
- [39] H. Hu, J. Hou, F. Zhang, and C. Zhang, Topological Triply Degenerate Points Induced by Spin-Tensor-Momentum Couplings, *Phys. Rev. Lett.* **120**, 240401 (2018).
- [40] L. Jin, X. Zhang, X. Dai, H. Liu, G. Chen, and G. Liu, Centrosymmetric Li_2NaN : A superior topological electronic material with critical-type triply degenerate nodal points, *J. Mater. Chem. C* **7**, 1316 (2019).
- [41] J. Wang, X. Sui, W. Shi, J. Pan, S. Zhang, F. Liu, S. Wei, Q. Yan, and B. Huang, Prediction of Ideal Topological Semimetals with Triply Degenerate Points in the NaCu_3Te_2 Family, *Phys. Rev. Lett.* **119**, 256402 (2017).
- [42] J. B. He, D. Chen, W. L. Zhu, S. Zhang, L. X. Zhao, Z. A. Ren, and G. F. Chen, Magnetotransport properties of the triply degenerate node topological semimetal tungsten carbide, *Phys. Rev. B* **95**, 195165 (2017).
- [43] J. Hou, Z. Li, X. Luo, Q. Gu, and C. Zhang, Topological Bands and Triply Degenerate Points in Non-Hermitian Hyperbolic Metamaterials, *Phys. Rev. Lett.* **124**, 073603 (2020).
- [44] Y. Xie, C. Gong, J. Zhou, X. Yan, and Y. Chen, Design triple points, nexus points, and related topological phases by stacking monolayers, *Appl. Phys. Lett.* **115**, 073105 (2019).
- [45] X. Feng, W. Wu, Y. Huang, Z. Yu, and S. A. Yang, Triply degenerate point in three-dimensional spinless systems, *Phys. Rev. B* **104**, 115116 (2021).
- [46] A. Das and S. Pujari, Topological character of three-dimensional nexus triple point degeneracies, *Phys. Rev. B* **102**, 235148 (2020).

- [47] X. Zhao, P. Guo, F. Ma, and Z. Lu, Coexistence of topological Weyl and nodal-ring states in ferromagnetic and ferrimagnetic double perovskites, *Phys. Rev. B* **103**, 085138 (2021).
- [48] E. Yang, B. Yang, O. You, H. Chan, P. Mao, Q. Guo, S. Ma, L. Xia, D. Fan, Y. Xiang, and S. Zhang, Observation of Non-Abelian Nodal Links in Photonics, *Phys. Rev. Lett.* **125**, 033901 (2020).
- [49] G. G. Pyrialakos, N. Schmitt, N. S. Nye, M. Heinrich, N. V. Kantartzis, A. Szameit, and D. N. Christodoulide, Symmetry-controlled edge states in the type-II phase of Dirac photonic lattices, *Nat. Commun.* **11**, 2074 (2020).
- [50] R. Tan, Z. Li, P. Zhou, Z. Ma, C. Tan, and L. Sun, Coexistence of Weyl and Type-II Triply Degenerate Fermions in a Ternary Topological Semimetal YPtP, *Phys. Status Solidi RRL* **13**, 1900421 (2019).
- [51] J. Sun, D. Zhang, and K. Chang, Coexistence of topological nodal lines, Weyl points, and triply degenerate points in TaS, *Phys. Rev. B* **96**, 045121 (2017).
- [52] X. Zhang, Z. Yu, X. Sheng, H. Yang, and S. A. Yang, Coexistence of four-band nodal rings and triply degenerate nodal points in centrosymmetric metal diborides, *Phys. Rev. B* **95**, 235116 (2017).
- [53] H. Jin, Y. Song, W. E. Pickett, and K. Lee, Noncentrosymmetric compensated half-metal hosting pure spin Weyl nodes, triple nodal points, nodal loops, and nexus fermions, *Phys. Rev. Mater.* **3**, 021201(R) (2019).
- [54] Y. Yang, H. Sun, J. Xia, H. Xue, Z. Gao, Y. Ge, D. Jia, S. Yuan, Y. Chong, and B. Zhang, Topological triply degenerate point with double Fermi arcs, *Nat. Phys.* **15**, 645 (2019).
- [55] J. Wang, Superconductivity in topological semimetals, *Natl. Sci. Rev.* **6**, 2 (2019).
- [56] Q. Guo, O. You, B. Yang, J. B. Sellman, E. Blythe, H. Liu, Y. Xiang, J. Li, D. Fan, J. Chen, C. T. Chan, and S. Zhang, Observation of Three-Dimensional Photonic Dirac Points and Spin-Polarized Surface Arcs, *Phys. Rev. Lett.* **122**, 203903 (2019).
- [57] B. Yang, Q. Guo, B. Tremain, L. E. Barr, W. Gao, H. Liu, B. Béri, Y. Xiang, D. Fan, A. P. Hibbins, and S. Zhang, Direct observation of topological surface-state arcs in photonic metamaterials, *Nat. Commun.* **8**, 97 (2017).
- [58] H. Zheng and M. Z. Hasan, Quasiparticle interference on type-I and type-II Weyl semimetal surfaces: a review, *Adv. Phys.* **X 3**, 1466661 (2018).
- [59] M. J. Park, B. Basa, and M. J. Gilbert, Disorder-induced phase transitions of type-II Weyl semimetals, *Phys. Rev. B* **95**, 094201 (2017).
- [60] Y. Fu and H. Qin, Topological phases and bulk-edge correspondence of magnetized cold plasmas, *Nat. Commun.* **12**, 3924 (2021).